

Abundances of carbon-enhanced metal-poor stars as constraints on their formation[★]

C.J. Hansen^{1,2}, B. Nordström^{1,3}, T.T. Hansen², C.R. Kennedy^{4,6}, V.M. Placco⁵, T.C. Beers⁵, J. Andersen^{1,3,7}, G. Cescutti^{8,9} and C. Chiappini⁸

¹ Dark Cosmology Centre, The Niels Bohr Institute, Juliane Maries Vej 30, DK-2100 Copenhagen, Denmark e-mail: cjhansen@dark-cosmology.dk, birgitta@nbi.ku.dk, ja@nbi.ku.dk

² Zentrum für Astronomie der Universität Heidelberg, Landessternwarte, Königstuhl 12, D-69117 Heidelberg, Germany e-mail: thansen@lsw.uni-heidelberg.de

³ Stellar Astrophysics Centre, Department of Physics and Astronomy, Aarhus University, Ny Munkegade 120, DK-8000 Aarhus C, Denmark

⁴ Research School of Astronomy and Astrophysics, Australian National University, Cotter Road, Weston, ACT 2611, Australia

⁵ Department of Physics and JINA Center for the Evolution of the Elements, University of Notre Dame, Notre Dame, IN 46556, USA e-mail: tbeers@nd.edu, vplacco@nd.edu

⁶ Department of Chemistry, Biochemistry, and Physics, University of Tampa, 401 W. Kennedy Blvd., Tampa, FL 33606, USA e-mail: ckennedy@ut.edu

⁷ Nordic Optical Telescope Scientific Association, Apartado 474, ES-38700 Santa Cruz de La Palma, Canarias, Spain

⁸ Leibniz-Institut für Astrophysik Potsdam (AIP), D-14482 Potsdam, Germany e-mail: cristina.chiappini@aip.de

⁹ Centre for Astrophysics Research, University of Hertfordshire, Hatfield, Herts, AL10 9AB, UK e-mail: g.cescutti@herts.ac.uk

Received August, 2015; accepted November

ABSTRACT

Context. An increasing fraction of carbon-enhanced metal-poor (CEMP) stars is found as their iron abundance, $[\text{Fe}/\text{H}]$, decreases below $[\text{Fe}/\text{H}] = -2.0$. The CEMP-*s* stars have the highest absolute carbon abundances, $[\text{C}/\text{H}]$, and are thought to owe their enrichment in carbon and the slow neutron-capture (*s*-process) elements to mass transfer from a former asymptotic giant-branch (AGB) binary companion. The most Fe-poor CEMP stars are normally single, exhibit somewhat lower $[\text{C}/\text{H}]$ than CEMP-*s* stars, but show no *s*-process element enhancement (CEMP-no stars). CNO abundance determinations offer clues to their formation sites.

Aims. Our aim is to use the medium-resolution spectrograph X-shooter/VLT to determine stellar parameters and abundances for C, N, Sr, and Ba in several classes of CEMP stars, in order to further classify and constrain the astrophysical formation sites of these stars.

Methods. Atmospheric parameters for our programme stars were estimated from a combination of $V-K$ photometry, model isochrone fits, and estimates from a modified version of the SDSS/SEGUE spectroscopic pipeline. We then used X-shooter spectra in conjunction with the 1D LTE spectrum synthesis code MOOG, and 1D ATLAS9 atmosphere models to derive stellar abundances, and, where possible, isotopic $^{12}\text{C}/^{13}\text{C}$ ratios.

Results. C, N, Sr, and Ba abundances (or limits) are derived for a sample of 27 faint metal-poor stars for which the X-shooter spectra have sufficient S/N ratios. These moderate resolution, low S/N ($\sim 10-40$) spectra prove sufficient to perform limited chemical tagging and enable assignment of these stars into the CEMP sub-classes (CEMP-*s* and CEMP-no). According to the derived abundances, 17 of our sample stars are CEMP-*s* and three are CEMP-no, while the remaining seven are carbon-normal. For four CEMP stars, the sub-classification remains uncertain, and two of them may be pulsating AGB stars.

Conclusions. The derived stellar abundances trace the formation processes and sites of our sample stars. The $[\text{C}/\text{N}]$ abundance ratio is useful to identify stars with chemical compositions unaffected by internal mixing, and the $[\text{Sr}/\text{Ba}]$ abundance ratio allows us to distinguish between CEMP-*s* stars with AGB progenitors and the CEMP-no stars. Suggested formation sites for the latter include faint supernovae with mixing and fallback and/or primordial, rapidly-rotating, massive stars (spinstars). X-shooter spectra have thus proved to be valuable tools in the continued search for their origin.

Key words. Stars: abundances – Stars: carbon – Stars: Population II – Stars: chemically peculiar – Nuclear reactions, nucleosynthesis, abundances

1. Introduction

The class of very metal-poor (VMP; $[\text{Fe}/\text{H}] < -2.0$) stars with strong molecular absorption features of carbon, in particular the CH *G*-band, are collectively referred to as carbon-enhanced metal-poor (CEMP) stars. They are defined as stars with $[\text{Fe}/\text{H}]$

≤ -2 and $[\text{C}/\text{Fe}] > 0.7$, following Beers & Christlieb (2005) and Aoki et al. (2007), respectively. For convenience, we employ the term “carbonicity” for the carbon-to-iron ratio, $[\text{C}/\text{Fe}]$, to distinguish it from the absolute carbon abundance, $[\text{C}/\text{H}]$ (Placco et al. 2011).

In the last two decades it has been recognized that roughly 20% of VMP halo stars exhibit carbonicities up to several orders of magnitude larger than Solar (Marsteller et al. 2005; Rossi et al. 2005; Lucatello et al. 2006), rising to 30% for stars with $[\text{Fe}/\text{H}] < -3.0$, 40% for $[\text{Fe}/\text{H}] < -3.5$, and 75% for

Send offprint requests to: C. J. Hansen, e-mail: cjhansen@dark-cosmology.dk

[★] Based on observations obtained at ESO Paranal Observatory, programmes 084.D-0117(A) and 085.D-0041(A)

$[\text{Fe}/\text{H}] < -4.0$. The handful of stars known with $[\text{Fe}/\text{H}] < -5.0$ all exhibit large carbonicities (Lee et al. 2013; Placco et al. 2014b; Frebel & Norris 2015), including the most iron-poor star presently known, SMSS J0313-6708, with $[\text{Fe}/\text{H}] < -7.8$ (Keller et al. 2014; Bessell et al. 2015). A definitive interpretation of this increasing frequency has not yet been found, but it has been argued (e.g., Carollo et al. 2012) that CEMP stars are more frequently associated with the outer-halo population of the Galaxy than with the inner-halo population, suggesting differences in the nucleosynthetic production sites of carbon in these components. Carollo et al. (2014) presented indications of the CEMP-*s* stars being preferentially associated with the inner-halo population, while the CEMP-no stars are associated with the outer-halo population. Based on these, and other recent results (see, e.g., Ito et al. 2013; Placco et al. 2014a; Hansen et al. 2015), it is becoming increasingly clear that the CEMP-no stars may well be bona fide second-generation stars, born from an ISM polluted with the nucleosynthetic products of the very first stars.

A few exceptions to this empirical rule have been presented in Bonifacio et al. (2015) and Caffau et al. (2011). In the former study, a star with an upper limit of $[\text{Fe}/\text{H}] < -5.0$ was found to have a low absolute C abundance, while the latter study presented a truly metal-poor star (SDSS J102918+172927), with metallicity slightly above $[\text{Fe}/\text{H}] = -5.0$ but without large carbonicity ($[\text{C}/\text{Fe}] \leq 0.9$).

In any event, most results indicate that significant amounts of carbon were produced already at the very earliest stages of the chemical evolution of the Milky Way and the Universe itself. The Galactic chemical evolution (GCE) models by Cescutti et al. (2013) can account for a large amount of the star-to-star scatter in $[\text{Sr}, \text{Ba}/\text{Fe}]$ found at the lowest $[\text{Fe}/\text{H}]$, and can provide good explanations for the chemistry of most CEMP-no stars, based on a spinstar production scenario (see Cescutti & Chiappini 2010). However, these models alone cannot simultaneously explain the large excess of C, N, and *s*-process elements found in the CEMP-*s* stars.

High-resolution spectroscopic studies have shown that $\sim 80\%$ of the known CEMP stars are CEMP-*s* stars (Aoki et al. 2007, based on their sample of 26 stars). The favoured mechanism to account for these stars is local transfer of carbon-rich material from the envelope of an asymptotic giant-branch (AGB) star to the surface of a surviving binary companion (e.g., Herwig 2005; Bisterzo et al. 2012). Correspondingly, detailed models for the chemical composition of a number of CEMP-*s* stars have been developed (e.g., Placco et al. 2013; Abate et al. 2015; Placco et al. 2015), but no definitive proof yet exists that they are *all* members of binary systems (although a great majority are clearly binaries, see, e.g., Lucatello et al. 2005; Starkenburg et al. 2014). If a given CEMP-*s* star is not a member of a binary system, eliminating the possibility of mass transfer from an evolved companion, the excess C must have been produced by a distant external source and implanted in the natal cloud of the star observed today.

CEMP-no stars are known to be particularly prevalent among the lowest-metallicity stars (Aoki et al. 2007). Indeed, of the nine stars known with $[\text{Fe}/\text{H}] \leq -4.5$, seven are CEMP-no stars (Placco et al. 2014b; Bonifacio et al. 2015; Frebel & Norris 2015), suggesting that C was produced and enriched already in the very first stellar generations. Their low binary frequency (Starkenburg et al. (2014); Hansen et al. 2015b, *subm.*), $\sim 17 \pm 5\%$, consistent with that of halo stars with normal carbon content, and their lack of *s*-process-element abundance signatures

makes a local AGB binary companion an unlikely source of their C excess, so another production site must be found.

One possible progenitor of the CEMP-no stars are massive, rapidly rotating, mega metal-poor ($[\text{Fe}/\text{H}] < -6.0$) stars (Meynet et al. 2006; Hirschi 2007; Frischknecht et al. 2012; Maeder et al. 2015), the so-called “spinstars”. Another suggested production site for the material incorporated into CEMP-no stars are the so-called “faint supernovae” associated with the first generations of stars, which experience extensive mixing and fallback during their explosions (e.g., Umeda & Nomoto 2003; Tominaga et al. 2007; Nomoto et al. 2013; Tominaga et al. 2014). It remains possible that both of these suggested progenitors may have played a role.

It is noteworthy that extremely metal-poor ($[\text{Fe}/\text{H}] \sim -3.0$) damped Lyman- α (DLA) systems at high redshift ($z = 2-3$) with enhanced $[\text{C}/\text{Fe}]$ (and other light elements) were recently reported by Cooke et al. (2011, 2012), indicating the existence of a C-enhanced ISM at very early times. Kobayashi et al. (2011) associate C and other elemental abundance signatures of CEMP-no stars with production by faint supernovae, and Matsuoka et al. (2011) have also argued for a strong carbon production in the early Universe, based on their analysis of the very distant radio galaxy TN 0924-2201 ($z = 5.19$)¹.

Progress on these issues requires as complete an inventory of the most important elemental- and isotopic-abundance ratios for CEMP stars as possible, in particular C, N, Fe, Sr, Ba, and $^{12}\text{C}/^{13}\text{C}$. The highly efficient X-shooter instrument on the ESO VLT, covering the full wavelength range from 300 nm to 2.3 μm range in a single exposure, allows us to measure the NH band, the CH band, Sr, and Ba in the near-UV to the optical and near-IR.

This paper reports our abundance analysis results for a sample of 27 MP or VMP stars, 20 of which are CEMP stars, and is outlined as follows. Section 2 discusses the target selection for our study. Details of our X-shooter observations are given in Sect. 3, while Sect. 4 describes our derivation of elemental abundances for the programme stars. Section 5 presents our results, while Sect. 6 offers a discussion of how our key results advance our ultimate goal of understanding the origin of CEMP stars. Finally, our conclusions are presented in Sect. 7.

2. Target selection

Our targets were selected from the “Catalogue of carbon stars found in the Hamburg-ESO survey” (Christlieb et al. 2001) and “Bright Metal-poor Stars from the Hamburg-ESO Survey” (Frebel et al. 2006). For this study we selected the brightest VMP stars, all of which are subgiants or giants, along with a number of additional chemically “normal” metal-poor stars. Initial estimates of atmospheric parameters for most of our candidates were available from application of a modified version of the SEGUE Stellar Parameter Pipeline (n-SSPP), described in more detail below. Based on these, we attempted to select objects in a temperature range suitable for estimation of molecular abundances such as those from molecular C and N bands. The X-shooter spectrograph remains efficient even at the NH band at 336 nm, so targets with an effective temperature down to ~ 4000

¹ Carbon ([CII]) is also measured at even higher redshifts ($z \sim 7.1$) in a quasar (J112001.48+064124.3), and is found to be lower than in other quasars at $z \sim 6$ (Venemans et al. 2012). The carbon-to-far infrared flux ratio indicate the presence of a significant amount of cold gas and dust in the early Universe.

K could be observed to a S/N ratio sufficient for abundance analysis in faint stars with reasonable integration times.

The list of our programme stars is given in Table 1, together with the integration times used and the S/N ratios obtained. The B and V magnitudes listed are from Beers et al. (2007) unless otherwise stated, while K ($= K_s$) and J magnitudes are from the 2MASS catalogue (Cutri et al. 2003). After our observations were already completed, the star HE 0430–1609 was found to be a single-lined spectroscopic binary with a period of the order of 3 years (Hansen et al. 2015c, *subm.*); this should not affect our results, as the low S/N we obtained for this star already yields larger uncertainties.

Our aim was to obtain spectra with sufficient S/N ratio around the NH band at 336 nm, guaranteeing a higher S/N in the redder parts of the wavelength range of X-shooter. However, measuring an actual S/N ratio from the spectra of cool stars in the near-UV is difficult, since the region is extremely crowded with molecular lines, and a clean continuum often cannot be defined. We have therefore measured the S/N in a region near 400 nm, which still contains a substantial number of (mostly) molecular lines (see Table 1). This S/N can be taken as representative of the spectrum quality near the Sr line that we employed.

3. Observations and data reduction

The X-shooter spectrograph is described by Vernet et al. (2011). It has three arms: UV (300–550 nm), visual (550–1000 nm) and near-IR (1000–2500 nm). Our observations were obtained in March and/or August 2010. We used slits of 1'', 0.9'' and 0.9'' in the three arms, yielding resolving powers $R = 4350, 7450$, and 5300 in the UV, visual, and near-IR spectral regions, respectively. The raw echelle spectra were reduced with the X-shooter pipeline², which is an automated routine that performs the necessary data-reduction steps, including merging of the orders. The one-dimensional output spectra were extracted, shifted to rest wavelength using cross-correlation with an accuracy of ± 1 km s⁻¹, and the continua were normalised in IRAF by dividing the spectra with a fitted pseudo-continuum using cubic splines or Legendre polynomials.

4. Stellar parameters and abundances

The determination of stellar parameters and derivation of stellar abundances were performed with the 1D LTE spectrum synthesis code MOOG (Snedden 1973, version 2014), using 1D interpolated Kurucz NEW-ODF, ATLAS9 model atmospheres (Castelli & Kurucz 2003), calculated with the interpolation code described by Allende Prieto et al. (2004).

4.1. Stellar atmospheric-parameter estimates

Extracting stellar atmospheric parameters from the spectra of stars that are dominated by dense forests of molecular bands and absorption lines, in particular for cool stars, is a challenging exercise. Most of the Fe lines normally used for determining [Fe/H] or microturbulence are either saturated or, at our resolving power ($R \sim 4350 - 7450$), so heavily blended that we are left with just a handful of usable Fe lines. This is too sparse to use the classical excitation and ionisation equilibrium techniques for atmospheric-parameter estimates, especially since the few useful Fe lines are limited to strong, low excitation-potential lines.

An obvious alternative tracer of [Fe/H] is the Ca triplet at ~ 855 nm. In our case the triplet lines are of dubious value, as the nearby TiO band is strong in most of our targets, interfering with the continuum placement in this region. Moreover, metallicities derived from the calibrations for red giant-branch stars by Cole et al. (2004) or for RR Lyrae by Wallerstein et al. (2012) are 0.2 – 1 dex lower than indicated by the few Fe lines we were able to measure. These apparently spuriously low metallicities resulted in poor spectral fits when synthesizing the stellar spectra using such metal-poor atmosphere models.

After much experimentation, we concluded that the best option was either to rebin the optical spectra so that they could be analyzed with techniques developed for lower resolution ($R \sim 2000$) spectra, such as those from SDSS, or else rely on the few useful Fe lines, as described below.

We estimated T_{eff} , $\log g$, and [Fe/H] using the n-SSPP, a modified version of the SEGUE Stellar Parameter Pipeline (SSPP, see e.g., Lee et al. 2008, 2013, for a detailed description of the methods employed). The n-SSPP uses low-resolution optical spectra (typically covering the wavelength range 380–550 nm), which we have for our programme stars, and photometric information (V_0 , $(B - V)_0$, J_0 , and $(J - K)_0$, corrected for extinction and reddening based on the Schlegel et al. 1998 dust maps), to determine first-pass estimates for each parameter – the [Fe/H] estimates being particularly important. Typical internal errors for the atmospheric parameters adopted by the n-SSPP are: 125 K for T_{eff} , 0.25 dex for $\log g$, 0.20 dex for [Fe/H], and 0.25 dex for [C/Fe]. External errors may well be larger, depending on the wavelength coverage and S/N ratio of the input spectra (see Beers et al. 2014, for further details). However, the n-SSPP pipeline fails for some stars in our sample (in particular those with very low S/N or $T_{\text{eff}} < 4500$ K, outside of the optimal range for the n-SSPP). In such cases, we are forced to derive the stellar parameters in other ways.

The temperatures were finally determined using $V - K$ and the IRFM-based calibrations of Alonso et al. (1999). The $E(B - V)$ were downloaded from the IRSA webpage using the stellar IDs; we adopted the mean $E(B - V)$ values from Schlegel et al. (1998). In the absence of usable trigonometric parallaxes for our stars, we applied the $\log g - T_{\text{eff}}$ scaling relation from Barklem et al. (2005). However, this relation yielded unrealistically low gravities for some of the stars; we therefore used isochrones, which in most cases agreed with the scaling relation to within 0.2 dex.

We have employed BaSTI (e.g., Pietrinferni et al. 2013) and Padova (Girardi et al. 2000) isochrones with the appropriate metallicities and C-N-O-enhancements to calculate surface gravities, adopting the photometric temperatures and [Fe/H] from the n-SSPP pipeline. Since the BaSTI isochrones resulted in somewhat larger values of $\log g$ for nine stars than expected from the n-SSPP pipeline, we adopted Padova isochrones for metallicities in the range $Z = 0.01 - 0.004$. A lower Z in the adopted isochrone leads to a lower gravity. The initial [Fe/H] estimates from the n-SSPP pipeline were adopted, and only adjusted if the strong Fe lines close to Sr and Ba (e.g., 406.3 and 407.1 nm) indicated a much lower or higher metallicity. In these instances we carried out a spectrum synthesis to fit these Fe lines and updated the [Fe/H] values accordingly. Since these Fe lines are strong, this approach may introduce a bias in our [Fe/H], but these lines remain detectable in our low-S/N, moderate-resolution spectra.

In summary, the stellar parameters were determined using photometry, Padova isochrones, and an [Fe/H] estimate based on a combination of the n-SSPP output and by fitting synthetic spectra to a few strong Fe lines near the Sr and Ba lines. The mi-

² Using the ESO common pipeline libraries version 5.1.0.

Table 1. Coordinates, photometry, integration times, and resulting S/N ratios for our programme stars

Name	RA	Dec	<i>B</i>	<i>V</i>	<i>J</i>	<i>K</i>	Int. Time [s]	S/N @4000Å
HE 0058–3449	01:01:21.6	-34:33:11	13.91	13.20	11.78	11.33	380	13
HE 0206–1916	02:09:19.6	-19:01:56	15.12	14.00	12.24	11.66	500	7
HE 0241–3512	02:43 26.7	-35:00:12	15.24	13.91	12.04	11.40	500	8
HE 0400–2030	04:02:14.8	-20:21:53	14.92	14.03	12.49	11.98	400	13
HE 0408–1733	04:11:06.0	-17:25:40	13.51	12.34	10.37	9.67	130	6
HE 0414–0343	04:17:16.4	-03:36:31	12.25	11.05	9.19	8.51	30	8
HE 0430–1609 ^{SB}	04:32:50.6	-16:03:38	14.41 ^a	13.21 ^a	11.39	10.74	230	6
HE 0430–4901	04:31:31.1	-48:54:42	15.16	14.57	13.31	12.81	250	36
HE 0440–3426	04:42:08.1	-34:21:13	12.59	11.42	9.65	8.97	60	10
HE 0448–4806	04:49:33.0	-48:01:08	13.39	12.78	11.59	11.21	400	17
HE 0516–2515	05:18:09.4	-25:12:25	15.44 ^a	13.66 ^a	11.25	10.35	600	10
HE 1238–0836	12:41:02.4	-08:53:06	13.56 ^A	11.79 ^A	9.19	8.15	400	9
HE 1315–2035	13:17:57.4	-20:50:53	16.81	15.43	13.68	13.05	1100	11
HE 1418+0150	14:21:01.2	01:37:18	14.05 ^a	12.33 ^a	9.99	9.13	600	9
HE 1430–0919	14:33:12.9	-09:32:53	15.68	14.31	12.48	11.86	800	10
HE 1431–0245	14:33:54.2	-02:58:33	16.59	15.22	13.57	12.99	800	11
HE 2138–1616	21:41:16.6	-16:02:40	14.81 ^A	13.68 ^A	11.90	11.32	350	9
HE 2141–1441	21:44:25.7	-14:27:33	14.53 ^A	13.37 ^A	11.40	10.73	280	8
HE 2144–1832	21:46:54.7	-18:18:15	12.65	11.14	8.77	7.96	30	6
HE 2153–2323	21:56:37.6	-23:09:25	16.21	14.67	12.53	11.74	700	8
HE 2155–2043	21:58:42.2	-20:29:15	13.92	13.16	11.57	11.02	300	40
HE 2235–5058	22:38:07.9	-50:42:42	13.83	12.92	11.43	10.89	200	10
HE 2250–4229	22:53:39.6	-42:13:03	12.66 ^A	11.91 ^A	10.40	9.87	100	30
HE 2310–4523	23:13:00.0	-45:07:06	12.12 ^A	11.21 ^A	9.44	8.81	40	30
HE 2319–5228	23:21:58.1	-52:11:43	14.15 ^A	13.25 ^A	11.55	10.96	450	20
HE 2357–2718	23:59:58.1	-27:01:37	14.31 ^A	13.08 ^A	11.09	10.42	170	6
HE 2358–4640	00:00:50.9	-46:23:31	14.39 ^A	13.67 ^A	12.15	11.64	500	22

Notes. Remarks: SB = single-lined spectroscopic binary.

^A = APASS (Henden et al. 2015); ^a = average of APASS and values in Beers et al. (2007).

croturbulence was estimated by applying the Gaia-ESO scaling relation between temperature, gravity, metallicity, and microturbulence (Bergemann et al. in prep.). This resulted in values typically between 1.5 and 2.0 km s⁻¹ for most stars. The adopted stellar parameters are thus more uncertain than those derived from high-resolution spectra, and these uncertainties will propagate into the derived stellar abundances (see Sect. 4.3). The final atmospheric parameters are listed in Table 2.

Line lists

Before synthetic spectra can be generated, line lists for all relevant features must be assembled. The line list for the molecular bands such as NH, CH, C₂, and CN are taken from Masseron et al. (2014) and T. Masseron (2015, priv. comm.). The adopted dissociation energies are 3.47 eV (CH), 3.42 eV (NH), 6.24 eV (C₂), and 7.7 eV (CN). The line list covering the atomic lines (Sr and Ba) are from Sneden et al. (2014), with the Sr hyperfine structure from Bergemann et al. (2012) and Hansen et al. (2013), and the Ba hyperfine structure (HFS) from Gallagher et al. (2012). Since most of these stars are of higher metallicities or enriched by an *s*-process, we used the total Solar System isotopic-abundance ratios for the heavy elements.

4.2. Derivation of molecular and atomic stellar abundances

With the ATLAS9 model atmospheres, the above line list, and the stellar parameters in Table 2, the synthetic spectra for each star were computed with MOOG and convolved with a Gaussian representing the X-shooter resolution at the appropriate wavelength.

Synthetic spectra of the CH *G*-band (430 nm) and C₂ Swan band (516 nm) were fit to the observations to derive the [C/Fe] abundance ratios of our stars, using χ^2 minimization for matching the synthetic and the observed spectra across a selected sensitive spectral interval. Nitrogen abundances were estimated in the same way, by fitting synthetic spectra to the NH band around 336 nm and CN around 389 nm and 421 nm, respectively. The listed abundances are average values of these measurements. The stars with low C or N rely only on the strongest CH or NH band, respectively.

The isotopic carbon ratios were derived by measuring molecular ¹³CH features in the range 421–423.5 nm.

Originally, we intended to obtain estimates of O from the CO bands in the near-IR, but the quality of the spectra obtained proved insufficient. We hope to obtain improved spectra in the future, from which another attempt to extract O abundances will be made.

The neutron-capture elements Sr and Ba are of particular interest for CEMP stars, as they enable us to distinguish between the CEMP-*s* and CEMP-no sub-classes. Both elements are detectable in the X-shooter spectra, due to their strong resonance lines (Hansen et al. 2013). Their abundances were derived via line-by-line spectrum synthesis with line lists including all relevant molecular and atomic lines, and taking into account the HFS of both the Sr and Ba lines. The Sr II line at 407.7 nm is the only useful line of Sr, as all other lines are either too weak or are obliterated by strong blends or molecular bands. However, this line is very strong and tends to saturate.

For Ba, we used the two lines at 455.4 nm and 585.3 nm, since they generally yield abundances in good agreement with each other. The 455.4 nm line is the strongest, and is usually

Table 2. Atmospheric parameters for the programme stars; ‘*u*’ indicates uncertain values.

Star	T_{eff} [K]	$\log g$ [cgs]	[Fe/H] [dex]	ξ [km s ⁻¹]
HE 0058–3449	5400	3.0	–2.1	1.5
HE 0206–1916	4800	1.4	–2.4	2.0
HE 0241–3512	4600	1.2	–1.8	2.0
HE 0400–2030	5200	2.5	–2.2	1.7
HE 0408–1733	4600	1.4	–0.8 ^u	1.7
HE 0414–0343	4700	1.3	–2.5	2.0
HE 0430–1609	4700	1.3	–2.3	2.0
HE 0430–4901	5500	3.3	–3.1	1.5
HE 0440–3426	4700	1.3	–2.6	2.0
HE 0448–4806	5800	3.4	–2.4	1.5
HE 0516–2515	4400 ^u	0.7	–2.5 ^u	2.2
HE 1238–0836	4100 ^u	0.1 ^u	–1.9	2.3
HE 1315–2035	5100 ^u	2.2 ^u	–2.5 ^u	1.8
HE 1418+0150	4200	0.6	–1.3 ^u	2.2
HE 1430–0919	4900	1.6	–2.5	1.9
HE 1431–0245	5200	2.3	–2.5 ^u	1.8
HE 2138–1616	4900	1.9	–0.5	1.6
HE 2141–1441	4600	1.4	–0.6	1.6
HE 2144–1832	4200	0.6	–1.7	2.2
HE 2153–2323	4300	0.6	–2.4 ^u	2.3
HE 2155–2043	5200	2.4	–3.0	1.5
HE 2235–5058	5200	2.5	–2.7	1.5
HE 2250–4229	5200	2.4	–2.7	1.7
HE 2310–4523	4700	1.4	–2.5	2.0
HE 2319–5228	4900	1.6	–2.6	2.0
HE 2357–2718	4500	1.3	–0.5	1.7
HE 2358–4640	5100	2.4	–1.7	1.6

detected even in the most metal-poor stars. The 585.3 nm line is weaker, and for that reason possibly more reliable when detectable. The 493.4 nm line is too blended and/or weak to yield reliable abundances, and it was only used to support the upper limit values estimated from the 455.4 nm line when the 585.3 nm line was too weak or blended. Line blends were taken into account by scaling the blends to the overall [Fe/H], α -, r - and s -process levels when deriving Sr and Ba abundances. Figure 1 shows our spectrum synthesis around the Sr and Ba lines for two programme stars.

4.3. Error propagation

The uncertainties listed in Table 4 indicate how well the stellar parameters could be determined, and in turn, how well the abundances could be derived. Several of the stars show signs of variability or are known binaries; in most cases these could not be fit as well as the constant VMP stars. The listed uncertainties on the temperature estimates take into account the variability (which could change the magnitudes and thereby the colour of the star) as well as uncertainties on the de-reddening. These uncertainties are folded into those on the gravities, where a good agreement between Padova and BaSTI isochrones, as well as an agreement between these and the n-SSPP and the scaled gravities are also taken into account (i.e., the standard deviation around the mean $\log g$ is considered as well). The uncertainties on the metallicity are estimated from a line-by-line synthesis of the clearly detectable Fe lines in the vicinity of Sr and Ba. The uncertainties have been rounded off in the same way as the stellar parameters.

At the resolving power in the blue arm of X-shooter ($R \sim 4350$) all the features of interest are blended to some extent. In particular, features within $\sim \pm 0.1$ nm, are blended into the two

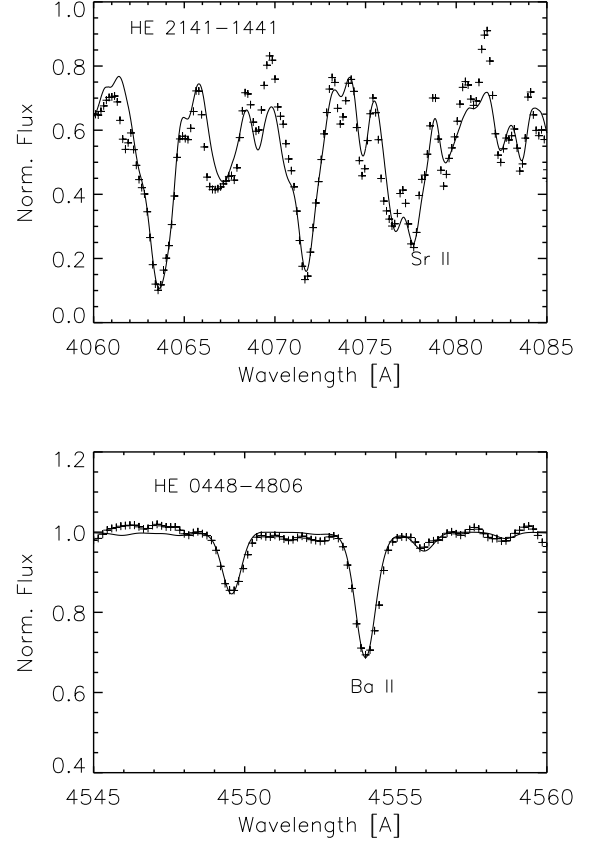


Fig. 1. Synthetic spectrum fits to the Sr II 407.7 nm (upper panel) and Ba II 455.4 nm lines (lower panel). The observations of HE 2141–1441 (relatively metal rich, s -element poor) and HE 0448–4806 (relatively metal poor, s -element rich) are shown as black plus signs.

Sr and Ba lines. These blends affect the Sr line (407.7 nm) the most, and we compensated for the blending by La and Dy lines by setting their abundances to that derived from Ba, and then adjusted this value by up to 0.3 dex to obtain a better fit of the Sr line.

A minimum abundance error of 0.1 dex due to blends, continuum placement, line list uncertainties, and overall spectrum quality is included in the total error budget, rising to 0.2 dex for the bluest regions of the lowest-quality spectra. For poor-quality spectra, the largest uncertainties are due to the stellar parameters ($T/\log g/[Fe/H]/\xi$: ± 300 K/ ± 0.3 dex/ ± 0.3 dex/ ± 0.3 km s⁻¹). In the following we describe our detailed analysis of the maximum abundance uncertainties caused by the stellar parameters for a spectrum of low quality (see Tables 2 and 3).

A minimum uncertainty was estimated using the best spectra and the best-constrained stellar atmospheric-parameter estimates, and is on the order of $T/\log g/[Fe/H]/\xi$: 100 K/ 0.2 dex/ 0.1 dex/ 0.15 km s⁻¹, similar to the uncertainty seen in high-resolution studies and corresponding to our best spectra with a S/N ratio > 30 . In this study, most of the stars actually have spectra with S/N ~ 10 at 400 nm, leading to larger errors. From the minimum and maximum uncertainties we calculated a mean representing the general abundance uncertainty for Sr and Ba.

As seen in Table 3, the temperature has the largest impact on the derived abundances. However, Sr and Ba are ionised,

Table 3. Abundance sensitivity to stellar parameters for HE 0400–2030.

Line	Sr 407.7 nm	Ba 455.4 nm	Ba 585.3 nm
Abundance:	[dex]	[dex]	[dex]
Parameter:			
$T \pm 300$ K	0.32	0.35	0.3
$\log g \pm 0.3$ dex	0.03	0.05	0.05
$[\text{Fe}/\text{H}] \pm 0.3$ dex	0.26	0.15	0.25
$\xi \pm 0.3$ km s ⁻¹	0.03	0.02	0.15
Max. uncert.:	0.41	0.38	0.42
Mean uncert.:	0.34	0.3	0.3

so gravity also influences the line strength, but less visibly due to the blends in the line wings. Microturbulence has the least impact on the Sr and 455.4 nm Ba lines, while the 585.3 nm line of Ba is clearly affected by this parameter. The difference in stellar-parameter sensitivity, combined with line blends and varying spectral resolution, explains the small difference in Ba abundances derived from the 455.4 nm line in the blue region ($[\text{Ba}/\text{Fe}] = 1.95$) and the 585.3 nm Ba line ($[\text{Ba}/\text{Fe}] \sim 1.7$) in the visual region. However, all the Sr and Ba lines agree on the presence or absence of any *s*-process enhancement, so a star remains enhanced whether or not we consider the blue or visual region of the spectrum.

Finally, we adopted a minimum error of 0.2 dex for the C and N abundances, dominated by the uncertainties in the atmospheric-parameter estimates.

5. Results

The derived abundances are listed in Table 4. The CEMP classification of Beers & Christlieb (2005), but adopting a lower limit of $[\text{C}/\text{Fe}] > 0.7$ as the criterion for CEMP stars (Aoki et al. 2007), leads to 17 CEMP-*s* stars, three CEMP-no stars, and seven carbon-normal metal-poor stars³ in the total sample. Some of the stars are difficult to fit owing to low S/N, binarity, or pulsations; these are identified by a “u” in the table to indicate that the results are more uncertain. The poorer fit to these stars is characterised from a larger standard deviation between the observations and the synthetic MOOG spectra in the range 406 – 409 nm.

5.1. C and N

In addition to the elemental abundances of C and N, we estimated carbon isotope ratios, $^{12}\text{C}/^{13}\text{C}$, for 13 of our programme stars from ^{13}CH lines in the range 421 – 423.5 nm; one CEMP-no and 12 CEMP-*s* stars (see Table 4).

All of the stars labelled as CEMP-*s* have $[\text{C}/\text{Fe}] > 0.7$ and $[\text{Ba}/\text{Fe}] > 1.0$, which rules out their association with the CEMP-no class. However, three stars exhibit weak Sr absorption lines and almost no Ba features. These are so faint that we can only provide upper limits ($[\text{Sr}, \text{Ba}/\text{Fe}] < -3$) in one case. These three CEMP-no stars are HE 2155–2043, HE 2250–4229, and HE 2319–5228, discussed in detail in Sect. 6.3. We also identify one very nitrogen-enhanced metal-poor (NEMP) star, HE 0400–2030.

All our programme stars have been checked against the data of Placco et al. (2014b) and Hansen et al. (2015), and the

³ Throughout the paper we refer to C-normal very metal-poor stars as VMP stars, which are to be distinguished from the C-enhanced CEMP stars.

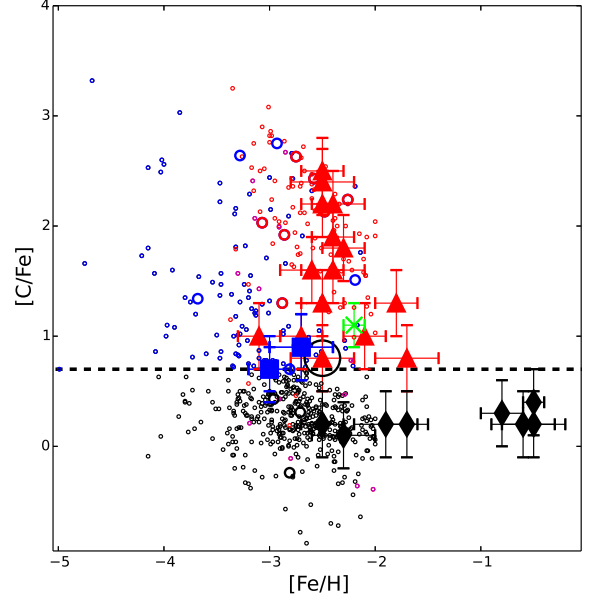


Fig. 2. $[\text{C}/\text{Fe}]$ vs. $[\text{Fe}/\text{H}]$ for our sample, compared to literature values: Hansen et al. (2015) (large, open circles) and Placco et al. (2014b) and references therein (small, open circles). CEMP-*s* stars are shown in red, CEMP-no stars in blue, the NEMP star in green, and carbon-normal MP stars in black. The dashed line at $[\text{C}/\text{Fe}] = 0.7$ separates the VMP and CEMP stars.

comparison samples used therein (Fig. 2). Figure 3 shows the $[\text{C}/\text{N}]$ abundance ratio for our programme stars. Two stars (HE 0400–2030 and HE 2319–5228; discussed in more detail in Sect. 6.3) are found to have mixed CNO-cycled material to their surfaces, converting some C into N (Spite et al. 2005, 2006), while C is normal or enhanced in the rest of the stars. We note that since most of our stars have relatively high gravities (and are subgiants), we do not expect that mixing would alter the surface composition of, e.g., C, and in most cases the C corrections⁴ from Placco et al. (2014b) are negligible (on the order of 0.0 – 0.03 dex). Even for such low-gravity stars as HE 2144–1832, the correction obtained is only ~ 0.13 dex. Therefore, we have not applied these corrections to any of our abundances.

A summary of our abundance results for C and N is shown in the two top panels of Fig. 4 as functions of $[\text{Fe}/\text{H}]$.

5.2. Sr and Ba

The Sr and Ba abundances help to distinguish the CEMP-*s* stars, which have presumably received C-enriched matter transferred from a former AGB companion (Lucatello et al. 2005), from the chemically normal VMP and CEMP-no stars. In contrast, the normal binary frequency of the CEMP-no stars (Starkenburg et al. (2014); Bonifacio et al. (2015) and Hansen et al. 2015b, subm.) suggests that their abundances reflect the composition of the gas from which they were born.

The derived abundances of Sr and Ba are shown as functions of $[\text{Fe}/\text{H}]$ in the two lower panels of Fig. 4, in which

⁴ Correction for stellar evolution effects that convert C into N.

Table 4. Final stellar parameters, C, N, Sr, and Ba abundances, $^{12}/^{13}\text{C}$ isotopic ratios, and CEMP classes.

Star	T_{eff} [K]	$\log g$ [cgs]	[Fe/H]	[C/Fe]	[N/Fe]	[Sr/Fe]	[Ba/Fe]	$^{12}/^{13}\text{C}$	CEMP class	Note
HE 0058–3449	5400 ± 200	3.0 ± 0.1	−2.1 ± 0.2	1.0 ± 0.2	1.1 ± 0.2	1.3 ^u ± 0.3	1.8 ± 0.2	9	s	
HE 0206–1916	4800 ± 200	1.4 ± 0.1	−2.4 ± 0.2	1.9 ± 0.2	1.1 ± 0.3	0.9 ± 0.2	1.3 ± 0.3	24	s	
HE 0241–3512	4600 ± 100	1.2 ± 0.1	−1.8 ± 0.2	1.3 ± 0.2	0.3 ± 0.2	1.6 ± 0.2	2.0 ± 0.2	9	(s)	
HE 0400–2030	5200 ± 200	2.5 ± 0.1	−2.2 ± 0.1	1.1 ± 0.2	2.5 ± 0.2	1.7 ± 0.2	2.0 ± 0.2	4	s	NEMP
HE 0408–1733	4600 ± 100	1.4 ± 0.3	−0.8 ± 0.3	0.3 ± 0.2	−0.6 ± 0.3	0.6 ± 0.2	0.2 ± 0.2	–	MP	
HE 0414–0343	4700 ± 100	1.3 ± 0.1	−2.5 ± 0.2	1.3 ± 0.2	1.6 ± 0.2	1.6 ± 0.2	1.9 ± 0.2	9	s	*,b (1)
HE 0430–1609	4700 ± 300	1.3 ± 0.2	−2.3 ± 0.2	1.8 ± 0.2	0.4 ± 0.3	1.6 ± 0.3	< 2.4	–	s	u,b (2)
HE 0430–4901	5500 ± 100	3.3 ± 0.3	−3.1 ± 0.2	1.0 ± 0.3	1.1 ± 0.3	1.0 ± 0.2	< 1.5	–	s	
HE 0440–3426	4700 ± 200	1.3 ± 0.2	−2.6 ± 0.3	1.6 ± 0.2	1.1 ± 0.2	0.9 ± 0.2	1.2 ± 0.2	9	s	
HE 0448–4806	5800 ± 200	3.4 ± 0.2	−2.4 ± 0.3	2.2 ± 0.2	1.2 ± 0.3	1.2 ± 0.2	2.3 ± 0.2	5	s	
HE 0516–2515	4400 ± 100	0.7 ± 0.3	−2.5 ± 0.3	> 0.8	–	0.5 ^u ± 0.3	0.5 ± 0.3	–	(s/no)	u,*
HE 1238–0836	4100 ± 300	0.1 ± 0.3	−1.9 ± 0.3	> 0.2	–	0.3 ^u ± 0.3	> −1.5	–	MP	u, R Sct (A)
HE 1315–2035	5100 ± 300	2.2 ± 0.3	−2.5 ± 0.2	2.5 ± 0.3	1.1 ± 0.2	1.6 ± 0.3	< 2.6	19	s	u
HE 1418+0150	4200 ± 100	0.6 ± 0.3	−2.3 ± 0.3	> +0.1	–	1.0 ± 0.3	> 1.0	–	MP(s)	u
HE 1430–0919	4900 ± 200	1.6 ± 0.2	−2.5 ± 0.1	2.2 ± 0.2	0.8 ± 0.3	1.0 ± 0.2	1.5 ± 0.3	32	s	
HE 1431–0245	5200 ± 200	2.3 ± 0.2	−2.5 ± 0.3	2.4 ± 0.2	1.5 ± 0.3	1.6 ± 0.2	1.9 ± 0.2	49	s	
HE 2138–1616	4900 ± 200	1.9 ± 0.3	−0.5 ± 0.3	0.2 ± 0.3	0.0 ± 0.3	0.7 ± 0.3	−0.4 ± 0.2	–	MP	u
HE 2141–1441	4600 ± 100	1.4 ± 0.3	−0.6 ± 0.3	0.2 ± 0.2	0.2 ± 0.3	0.5 ^u ± 0.3	0.1 ± 0.3	–	MP	
HE 2144–1832	4200 ± 100	0.6 ± 0.3	−1.7 ± 0.3	0.8 ± 0.2	0.6 ± 0.2	1.5 ± 0.2	1.3 ± 0.2	–	(s)	CH star (A)
HE 2153–2323	4300 ± 100	0.6 ± 0.2	−2.4 ± 0.3	1.6 ± 0.2	0.7 ± 0.3	1.2 ± 0.2	1.1 ± 0.2	12	s	
HE 2155–2043	5200 ± 100	2.4 ± 0.2	−3.0 ± 0.2	0.7 ± 0.2	0.0 ± 0.2	0.2 ± 0.2	–	–	no	*
HE 2235–5058	5200 ± 100	2.5 ± 0.2	−2.7 ± 0.2	1.0 ± 0.2	1.0 ± 0.2	1.7 ± 0.2	2.4 ± 0.2	32	s	
HE 2250–4229	5200 ± 100	2.4 ± 0.2	−2.7 ± 0.3	0.9 ± 0.3	0.4 ± 0.3	−0.3 ± 0.2	−0.3 ± 0.2	–	no	
HE 2310–4523	4700 ± 200	1.4 ± 0.2	−2.5 ± 0.2	0.2 ± 0.3	0.0 ± 0.3	0.0 ^u ± 0.3	−0.4 ± 0.2	–	VMP	
HE 2319–5228	4900 ± 100	1.6 ± 0.2	−2.6 ± 0.2	1.7 ± 0.2	2.5 ± 0.2	< −3	< −3	5	no	
HE 2357–2718	4500 ± 100	1.3 ± 0.3	−0.5 ± 0.1	0.4 ± 0.3	−0.1 ± 0.3	0.3 ± 0.2	−0.3 ± 0.2	–	MP	
HE 2358–4640	5100 ± 200	2.4 ± 0.1	−1.7 ± 0.2	0.2 ± 0.3	−0.1 ± 0.3	0.1 ± 0.2	−0.3 ± 0.3	–	MP	*

Notes. (*) Stellar parameters agree with values from n-SSPP pipeline.^(b) Spectroscopic binary. ^(u) Uncertain values.^(A) Possibly an AGB star.⁽¹⁾ Binary according to Hollek et al. 2015 (accepted).⁽²⁾ Binary according to Hansen et al. 2015c, (submitted).

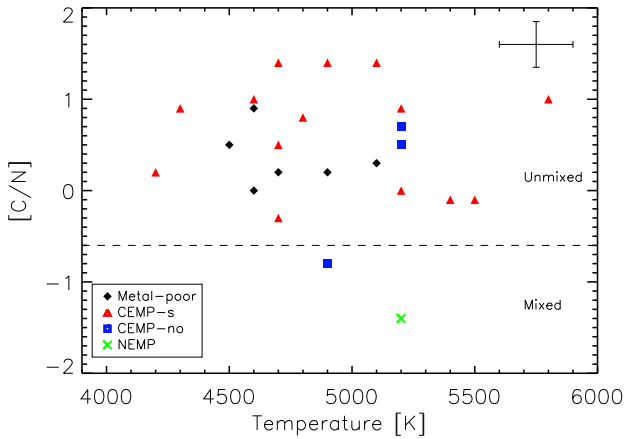


Fig. 3. [C/N] ratios determined from our X-shooter spectra. C-normal MP stars are shown as black diamonds and CEMP-*s* and CEMP-*no* as red triangles and blue squares, respectively, while the green cross shows the NEMP star. The dashed line indicates the limit below which CNO-cycled material has been mixed to the surface.

the metal-poor stars $[\text{C}/\text{Fe}] < 0.7$) are identified by black symbols. At $[\text{Fe}/\text{H}] < -1.5$, clear divisions of the Sr and Ba abundances into two branches are seen. Here, the span in Sr and Ba abundances at the lowest $[\text{Fe}/\text{H}]$ values amounts to ~ 3 dex (as also found in Hansen et al. 2012), corresponding to the dif-

ference between the chemically normal and CEMP-*no* stars on the one hand, and the highly enhanced CEMP-*s* stars on the other⁵. Between the branches is the CEMP-*no/s* star (for a definition see Sivarani et al. 2006) HE 0516–2515, with $[\text{Ba}/\text{Fe}] = 0.5$ and $[\text{Fe}/\text{H}] = -2.5$. Our X-shooter results for this star are uncertain, and higher-resolution observations are required to classify it with confidence. The blue data points on the low-Sr branch in Fig. 4 are the CEMP-*no* stars HE 2155–2043 and HE 2250–4229, while HE 2319–5228 falls below this branch. Except for HE 2319–5228, the CEMP-*no* stars have relatively low $[\text{C}/\text{Fe}]$ compared to the CEMP-*s* stars.

5.3. Comparison to literature

We have several stars in common with previous studies. Our temperatures generally agree within 150 K with those presented in Goswami (2005), Goswami et al. (2010), and Kennedy et al. (2011). The light-element (C, N) abundances agree within 0.2 dex, while larger differences (up to 0.4 dex) are found among the heavy-element abundances. This large difference can be accounted for by differences in the adopted gravities and metallicities, line lists, and continuum placement. The low resolution of the spectra classified in the study by Goswami et al. (2010) prevented them from deriving accurate metallicities; they estimated these values by comparing the spectra of their high-latitude stars to those with better-known parameters.

⁵ Mass transfer from a binary companion seems to be the only efficient way to change the surface composition of the CEMP-*s* stars to the observed levels.

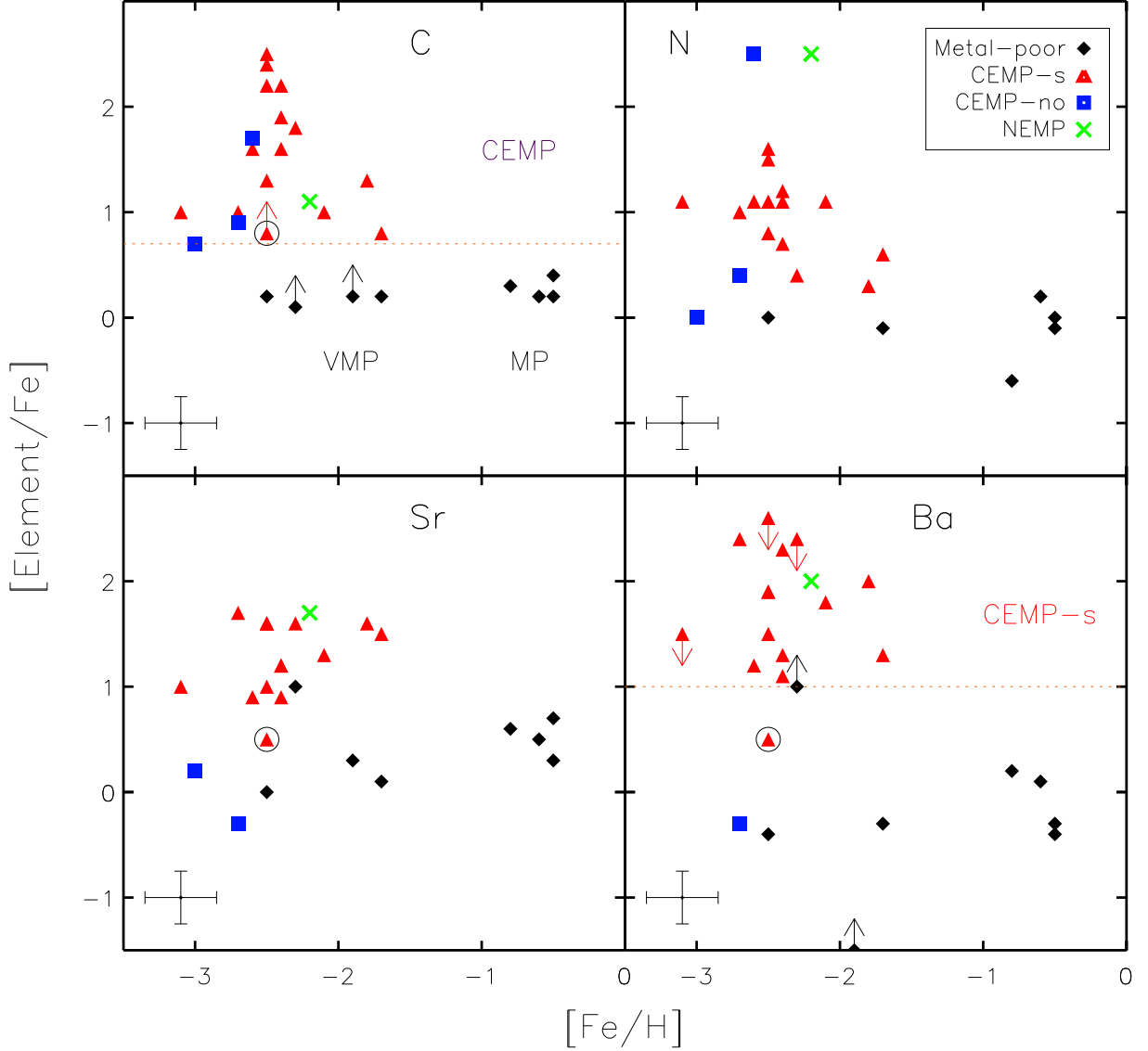


Fig. 4. [C, N, Sr, Ba/Fe] ratios vs. [Fe/H] for our programme stars. Chemically normal ($[C/Fe] < 0.7$) stars are shown in black; red triangles represent CEMP-*s* stars, and blue squares are CEMP-no stars, and the green 'x' symbol is the single NEMP star, respectively. The circle marks the uncertain CEMP-no/-*s* star HE 0516-2515. Dotted lines at $[C/Fe] = 0.7$ and $[Ba/Fe] = 1.0$ separate the VMP from the CEMP(-*s*) stars.

Our metallicities also generally agree with those presented in Kennedy et al. (2011) and Aoki et al. (2007), within 0.3 dex. The latter study is based on a high-resolution spectral analysis, compared to which we find fair agreement between most of our results except from the temperatures (owing to differences in adopted $E(B - V)$ values).

All abundances and other parameters derived for HE 1238-0836 are uncertain. The spectra for this star are of low quality, and furthermore, they resemble those of variable RV Tau-type stars⁶ according to Goswami et al. (2010). The pulsations in such a star can lead to large amplitude (and thus magnitude) changes depending on sub-class. Such variations

would in turn lead to very different stellar parameters and abundances, depending on whether the star was observed in an expanding or contracting phase.

Goswami et al. (2010) listed temperatures in the range between 3500 and 4000 K for HE 1238-0836. If the star were as cool as 3500 K when observed with X-shooter, we would expect to see very strong TiO bands in the red spectra (as in M dwarfs), which we do not. Based on the line profiles (Balmer lines as well as Ba lines) we believe that the star has not been observed at a quiet phase, but we need higher-resolution observations during this phase to improve our abundance measurements.

⁶ Since the star is bright, it may belong to the bright sub-class R Sct.

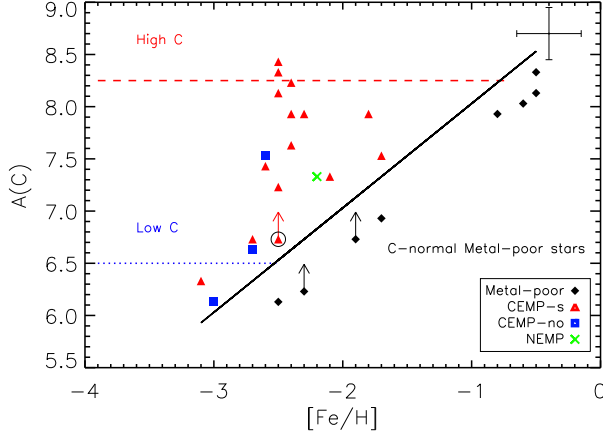


Fig. 5. Absolute carbon abundances, $A(C) = \log \epsilon(C)$, of our programme stars, as a function of metallicity, $[Fe/H]$. The high-C and low-C bands of Spite et al. (2013) are indicated by the horizontal lines. The Asplund et al. (2009) solar abundance of carbon, $\log \epsilon = 8.43$, has been assumed.

6. Discussion

The recent study of CEMP stars by Spite et al. (2013) showed that, depending on the level of absolute carbon abundance, the stars split into two bands (which they referred to as “plateaus”), where the strongly C-enhanced stars are typically CEMP-*s* stars, while the relatively less C-enriched stars are CEMP-no stars. Several studies have confirmed the existence of the carbon bands, and have populated them with more stars (e.g., Bonifacio et al. 2015; Hansen et al. 2015). Here we discuss the behaviour of the heavy elements, and how they associate with these bands, in order to better constrain the astrophysical sites and processes that enriched the different sub-classes of CEMP stars. Finally, since our sample also contains carbon-normal VMP stars, we comment on similarities and differences in the formation of VMP stars vs. CEMP stars.

Figure 5 shows the absolute C abundances for our programme stars, as a function of metallicity, $[Fe/H]$. The VMP stars are located below the $[C/Fe] = 0.7$ line. Roughly half of the CEMP-*s* stars lie close to the high-C band ($A(C) = 8.25$), while two of our CEMP-no stars are close to the low-C band ($A(C) = 6.25$). The other CEMP-no stars, the NEMP star, and a few CEMP-*s* stars, fall between the two bands. We do not find any of our programme CEMP-no stars located near the high-C band. Our results, as well as those from other larger studies indicate that there may exist a continuum of absolute C abundances lying between the high-/low-C bands, blurring their distinction.

A discontinuity is seen in both panels of Fig. 6, which illustrates the separation of CEMP-*s* vs. CEMP-no and VMP stars. The large difference in neutron-capture abundance of 1–2 dex found between C-normal VMP and CEMP-no stars and the CEMP-*s* stars explains some of the large star-to-star scatter found at low metallicity. This scatter has been found in numerous previous studies, and points towards differences in the formation sites and/or processes involved, if these are assumed to be robust and produce similar amounts of heavy elements in each event (see, e.g., Hansen et al. 2014).

Figure 7 compares the X-shooter measurements of the $[Sr/Fe]$, $[Ba/Fe]$, and $[Ba/Sr]$ abundance ratios for our programme stars to larger samples with high-resolution determi-

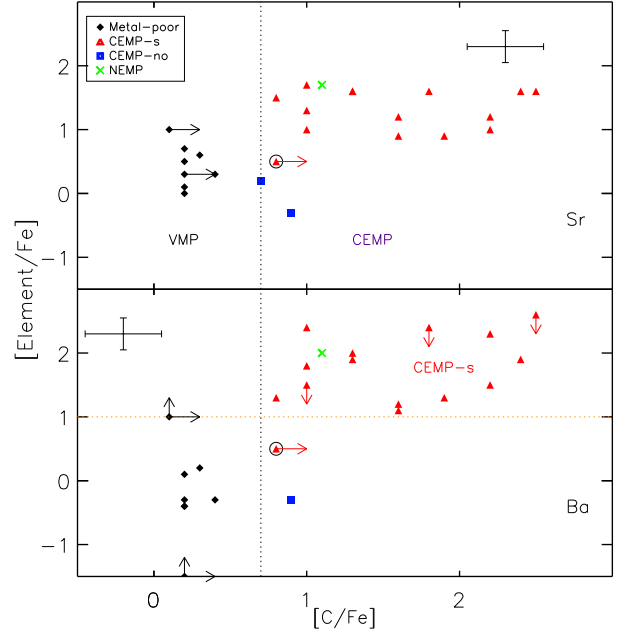


Fig. 6. $[Sr/Fe]$ (top) and $[Ba/Fe]$ (bottom) vs. $[C/Fe]$. The dashed line in the lower panel indicates the limit for *s*-process enhanced stars at $[Ba/Fe] > 1.0$. The vertical line at $[C/Fe] = 0.7$ separates VMP from CEMP stars.

nations from Hansen et al. (2012), Placco et al. (2014b), and Hansen et al. (2015). As seen from these figures, the CEMP-no stars follow the general trend of stars without C-enhancement predicted by standard Galactic chemical evolution (GCE) models, while the CEMP-*s* stars increase the star-to-star scatter, not just at extremely low metallicities, but over the entire range of $[Fe/H]$. This is confirmed by the Ba-Sr relation seen in Fig. 9, a relation also found by Roederer (2013) for a much larger sample.

Both VMP stars as well as CEMP stars exhibit a steady increase in their neutron-capture elements as a function of time (or $[Fe/H]$). Figure 8 shows this trend very clearly, in terms of the absolute Sr, Ba, and C abundances. Iron has intentionally been excluded in these figures, since Fe is formed in larger amounts by SNe of type Ia, which cannot explain the formation of CEMP-no (or CEMP-*s*) stars. A possible formation site of the early CEMP-no stars is faint core-collapse SN (type II), which might explode with an O-Ne-Mg core only (e.g., Wanajo et al. 2011), indicating that they will not produce a significant amount of iron. Thus, iron (and its formation processes) might confuse such trends, where we look for similarities in abundance ratios to trace the underlying formation process.

Figure 9 shows a difference in the neutron-capture element abundance trends between the C-normal VMP and CEMP-no stars compared to the CEMP-*s* stars. This would be expected if CEMP-*s* stars were enriched by a nucleosynthesis process that differs from that responsible for enriching metal-poor stars of similar $[Fe/H]$, but lower C-enhancement. The CEMP-*s* stars are also shown to contain more Ba (a main *s*-process elements) than Sr (a weak *s*-process element), yielding a lower $[Sr/Ba]$ ratio and pointing towards early AGB enrichment in a binary system (Lucatello et al. 2005; Masseron et al. 2010; Cristallo et al. 2011; Bisterzo et al. 2012; Starkenburg et al. 2014).

The CEMP-*s* stars in the top panel of Fig. 9 fall below the Ba-Sr 1:1 relation, while the VMP stars fall above – an indication

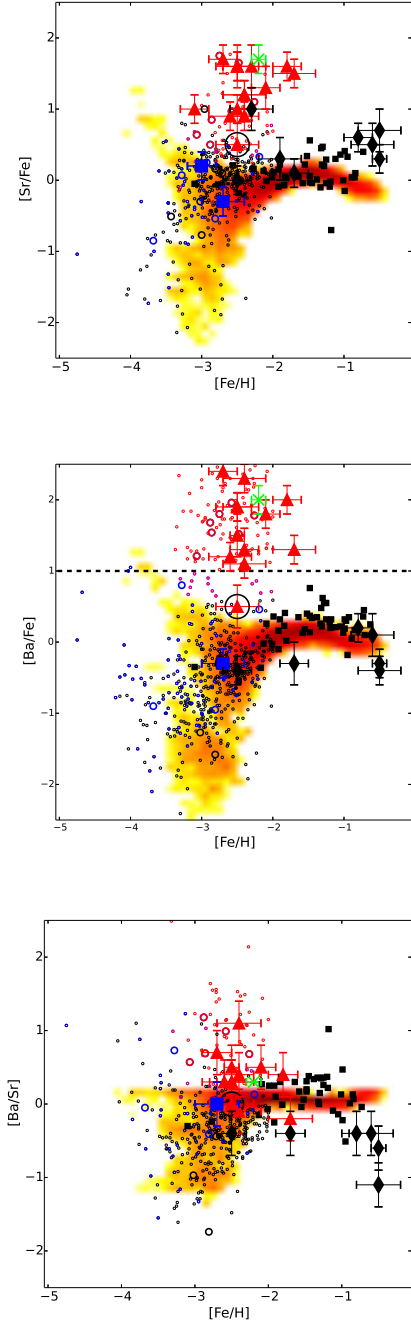


Fig. 7. Neutron-capture element abundances vs. $[\text{Fe}/\text{H}]$ for our stars compared to metal-poor star samples from Hansen et al. (2012, black squares), Hansen et al. (2015, large, open circles), and Placco et al. (2014b) and references therein (small, open circles), respectively. Colours and symbols as in Fig. 2. The red-yellow cloud shows the GCE predictions, where the red colour indicates a larger number density of stars than the yellow. The dashed line at $[\text{Ba}/\text{Fe}] = 1.0$ in the lower panel separates carbon-normal from CEMP-*s* stars. The bottom panel shows $[\text{Ba}/\text{Sr}]$ vs. $[\text{Fe}/\text{H}]$.

of different formation scenarios that could be hidden in the large star-to-star abundance scatter of Sr and Ba. The CEMP-no stars fall in-between these two groups, right on the 1:1 relation.

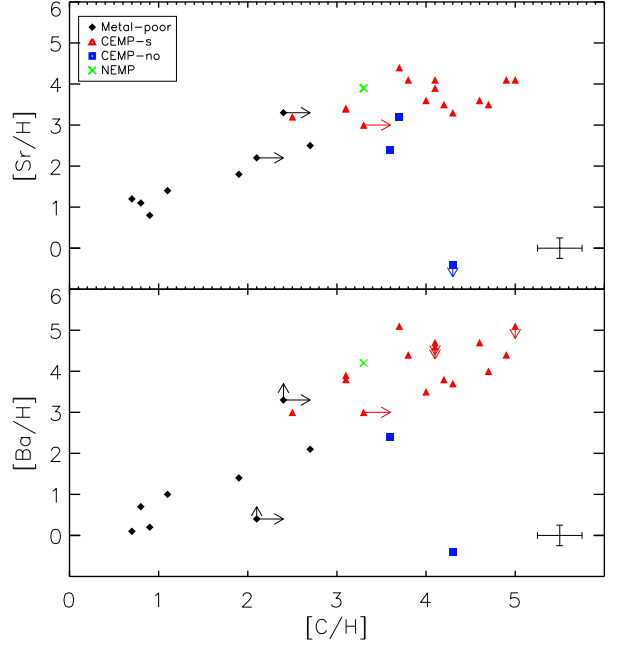


Fig. 8. $[\text{Sr}/\text{H}]$ vs. $[\text{C}/\text{H}]$ (top) and $[\text{Ba}/\text{H}]$ vs. $[\text{C}/\text{H}]$ (bottom). The outlier is HE 2319–5228.

The ratio of Sr and Ba can be used to trace the formation site – AGB stars vs. spinstars or faint SN II – and the $[\text{Ba}/\text{Sr}]$ value can even provide insight into the actual mass of the donor AGB star. The predicted $[\text{hs}/\text{ls}]$ ratio⁷ from a metal-poor AGB star of $1.5\text{--}2M_{\odot}$ is ~ 0.5 , according to the F.R.U.I.T.Y. database (Cristallo et al. 2011). Within the observational uncertainty, this is in fair agreement with the observed $[\text{Ba}/\text{Sr}]_{\text{average}} \sim 0.45$, based on all CEMP-*s* stars in Fig. 9 (dashed red line). The C-normal VMP stars show the opposite trend ($[\text{Ba}/\text{Sr}]_{\text{average}} \sim -0.55$; dotted black line). This element ratio could be created by fast-rotating stars, which might produce some Sr and little Ba, depending on conditions such as the rotation velocity (Frischnecht et al. 2012; Piersanti et al. 2013; Cristallo et al. 2015).

These relations are in good agreement with Galactic chemical evolution predictions (Fig. 7), where yields from spinstars may explain the chemically normal stars, but not stars with extreme *s*-process enhancements (Cescutti et al. 2013; Hansen et al. 2013).

6.1. Comparison to Galactic Chemical Evolution (GCE) models

Figure 7 shows the results from the GCE model presented in Cescutti et al. (2013). These results are based on the stochastic enrichment of the ISM, assuming that the pollution by stars are mixed only inside volumes with the radius of a typical SN II bubble (see Cescutti 2008). This model assumes *s*-process production by spinstars for Sr and Ba, responsible mainly for the region of low $[\text{Sr}/\text{Fe}]$ and $[\text{Ba}/\text{Fe}]$ at $[\text{Fe}/\text{H}] < -2.0$, coupled with a production of neutron-capture elements by an *r*-process in electron-capture SNe. By combining yields from these forma-

⁷ The logarithmic abundance ratio of heavy-to-light $[\text{hs}/\text{ls}]$ *s*-process elements, where we here use $[\text{Ba}/\text{Sr}]$ as an indicator.

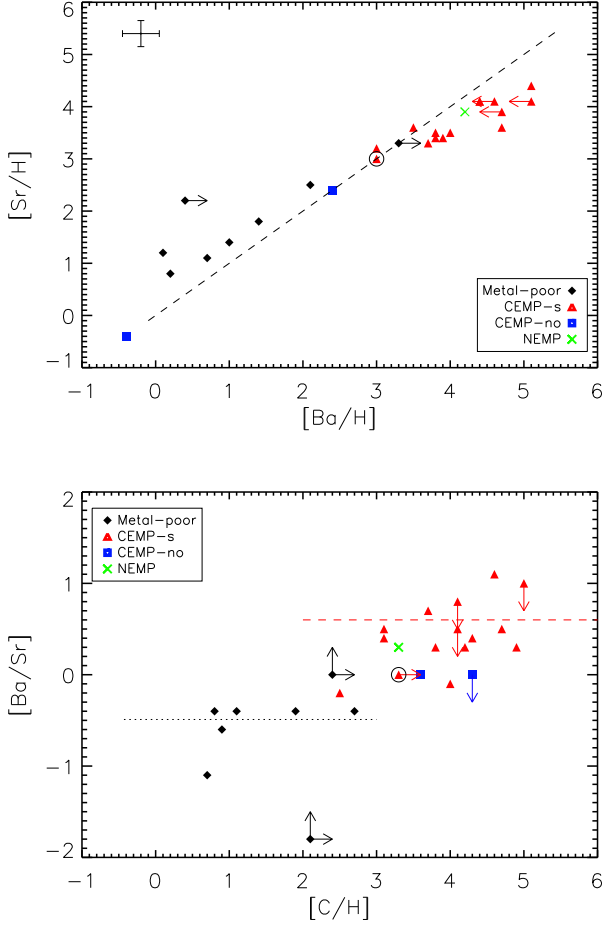


Fig. 9. Top: [Sr/H] as a function of [Ba/H], bottom: [Ba/Sr] as a function of [C/H]. Note the offset in the trends between VMP and the CEMP stars. Two stars in the bottom panel (one VMP and one CEMP-s,) lie between the two levels at [C/H] \sim 2.5; these are the two variable AGB star candidates. The dashed and dotted lines indicate the average [Ba/Sr] ratios of the two groups of stars (see text).

tion sites, the model can account for the dispersion of the data in [Sr/Fe] and [Ba/Fe] for normal stars (and CEMP-no stars)⁸.

Fig. 7 (bottom panel) highlights the importance of the production by spinstars of Sr and Ba at low metallicity coupled with an r -process production. In fact, not only rotating massive stars at low metallicity can produce a modest amount of Sr and Ba (compared to the production of an r -process event), but - even more interesting - this s -process production has an [Ba/Sr] ratio varying between 0 and -1.5 . As the predictions of the stochastic chemical evolution model show, this represents also a solution for the observed dispersion in [Ba/Sr] present in normal stars at extremely low metallicity.

As mentioned above, the chemical evolution model follows the Galactic halo ISM, and therefore cannot predict the enrichment observed in CEMP-s stars. In any case, their atmospheres

⁸ We note that these results are independent of other proposed r -process sites (see, e.g., Cescutti & Chiappini 2014) combined with spinstars. This was confirmed in Cescutti et al. (2015) using neutron star mergers as an r -process site. Similar results can be obtained considering only two different primary (r -)process contributions not involving spinstars (see, e.g., Hansen & Primas 2011; Hansen et al. 2014).

do not reflect the abundances of the ISM where these stars are formed, since the original chemical composition is altered by mass transfer from a binary companion, the most likely formation scenario for the majority of these objects.

6.2. Carbon isotopic ratios, $^{12}\text{C}/^{13}\text{C}$

Convection, either in AGB stars or in spinstars, drives the CNO cycle and transports ^{13}C and N, created at the expense of ^{12}C , to a star's surface. This is detectable in the isotopic abundance ratios of C and N, where low $^{12}\text{C}/^{13}\text{C}$ and [C/N] ratios indicate strong internal mixing with CN-cycled material (Spite et al. 2005). For 13 of our programme CEMP stars we find ratios that cover $3 < ^{12}\text{C}/^{13}\text{C} < 50$, where the higher end of this range is in good agreement with Bisterzo et al. (2011, 2012), who find that their AGB models do not result in strongly mixed material ($4 < ^{12}\text{C}/^{13}\text{C} < 10$).

The equilibrium value of $^{12}\text{C}/^{13}\text{C}$ for CNO-cycled material is 3-4, so stars with $^{12}\text{C}/^{13}\text{C} = 5$ indicate a high level of processing. This either points towards more processing in the AGB stars than current models predict, or it indicates processing by the star itself. Seven stars (HE 0058-3449, HE 0241-3512, HE 0400-2030, HE 0414-0343, HE 0440-3426, HE 0448-4806, HE 2319-5228) exhibit $^{12}\text{C}/^{13}\text{C}$ ratios < 10 ; two of these are subgiants and five are giants, in which some degree of internal processing is expected. We recall from Fig. 3 that HE 0400-2030 and HE 2319-5228 showed clear signs of mixing.

HE 1238-0836 and HE 2144-1832

Two stars stand out by having a low $\log g$ and a positive [C/N] ratio, namely HE 1238-0836 and HE 2144-1832. Both of these stars are also photometric variables. According to Goswami et al. (2010), HE 1238-0836 is an RV Tau-type (R Sct) star; such stars can exhibit extreme variations in their light curves. As mentioned in Sect. 5.3, we expect to have observed the star in (or close to) an expansion phase, where the gravity and in turn the pressure-sensitive abundances are too low. Multi-epoch follow-up observations would be needed to verify the variable character. We need to observe the star in a quiet phase, during which the derived stellar parameters and abundances can be trusted. However, there is also another possibility. Both stars could be pulsating, intrinsic AGB stars such as CS 30322-023 (Masseron et al. 2006) and HD 112869 (Začs et al. 2015). This would explain their low gravities and the fact that both stars are bright (brighter than most other stars in our programme). Either option could lead to [C/N] > 0 , and would most likely result in high $^{12}\text{C}/^{13}\text{C}$ -ratios.

6.3. CEMP-no and NEMP stars

To date we know ~ 80 CEMP-no stars (most of which have been included in Placco et al. 2014b)⁹. Not all of these are confirmed CEMP-no stars, but the majority are expected to belong to this sub-class. Our confirmation of three new CEMP-no stars (HE 2155-2043, HE 2250-4229, and HE 2319-5228) adds to this sample. The nature of the progenitors that enriched the ISM

⁹ Many studies over the past decades have steadily added to this sample, e.g.: Norris et al. (1997); Christlieb et al. (2002); Frebel et al. (2005); Aoki et al. (2007); Norris et al. (2007); Ito et al. (2013); Yong et al. (2013); Keller et al. (2014); Placco et al. (2014b); Bonifacio et al. (2015); Hansen et al. (2015); Li et al. (2015).

from which such stars formed (faint SNe with mixing and fallback, and/or spinstars) is still not fully understood.

In the spinstars scenario, rotation triggers mixing processes inside the star, and this leads to the production of important quantities of primary ^{14}N , ^{13}C , and ^{22}Ne compared to stellar evolution models without rotation (Hirschi 2007). However, this scenario does not fit the abundance pattern of one of the most-studied CEMP-no stars, BD+44°493 (Ito et al. 2013; Placco et al. 2014a; Maeder & Meynet 2015). Ito et al. (2013) found a nitrogen enhancement in this star that is too low with respect to the carbon enhancement to match these predictions. The abundance pattern of HE 2319–5228, however, appears to be consistent with a spinstar progenitor that may have been present in the earliest generations of stars (e.g., Maeder et al. 2015).

The NEMP star: HE 0400–2030

Johnson et al. (2007) defined the nitrogen-enhanced metal-poor (NEMP) stars as objects with $[\text{C}/\text{N}] \lesssim -0.5$ and $[\text{N}/\text{Fe}] > 0.5$, and found five examples. This number was lower than expected, and seemed to point towards an observational bias against discovering NEMP stars relative to CEMP stars (which are more readily identifiable from objective-prism surveys). However, the number of recognized NEMP stars has increased to ~ 45 at present (Placco et al. 2014b), which is a substantial number, although still less than the number of known CEMP-no and CEMP-*s* stars. We find one new NEMP star: HE 0400–2030, which has $[\text{C}/\text{N}] = -1.4$ and is also *s*-process-element enhanced.

6.4. Comparison to AGB yields

Due to hot-bottom-burning (HBB), the higher-mass stars (of $4 - 6 M_{\odot}$) produce prodigious amounts of nitrogen at the expense of carbon. A few CEMP stars studied to date exhibit abundance patterns that could be consistent with these higher-mass AGB stars, but the stars in our X-shooter sample appear to be largely consistent with the $1.5 - 3 M_{\odot}$ cases, where nitrogen is not enhanced relative to carbon, as would be expected from a HBB scenario.

Among the seven stars that show indications of mixing through their $[\text{C}/\text{N}]$ ratios or isotopic carbon-abundance ratios, none exhibit $[\text{C}/\text{N}] < -0.5$ and $[\text{hs}/\text{ls}] > 0.5$ simultaneously. This indicates that HBB in more massive stars ($\gtrsim 4 M_{\odot}$) is a less plausible explanation for the chemical composition of these stars. Most of our programme stars exhibit signs of weak internal mixing, which, based on their $[\text{Ba}/\text{Sr}]$ ($[\text{hs}/\text{ls}]$) ratios, can be explained by either AGB stars, massive spinstars, or faint SNe with mixing and fallback.

7. Conclusions

Twenty-seven stars from our X-shooter programme were analysed through spectral synthesis of molecular C and N bands, as well as atomic Ba and Sr lines. With only these four abundances, it is possible to classify each star according to its abundance pattern (i.e., CEMP-*s*, CEMP-no etc.). The majority of the known CEMP stars are enriched in *s*-process elements such as Ba and Sr. These CEMP-*s* stars appear to belong to the relatively metal-rich inner-halo population, while the CEMP-no stars may belong primarily to the relatively more metal-poor outer-halo population (e.g., Carollo et al. 2012, 2014).

Despite intense efforts to date, we are still trying to understand the exact formation sites of the CEMP-no and NEMP stars. Two of our newly confirmed CEMP-no stars appear to fall on (or

slightly above) the low-C band suggested by Spite et al. (2013). We also confirm the differences found between the strongly C-enhanced CEMP-*s* stars and the relatively less C-enhanced CEMP-no stars discussed by the same authors. However, several stars in this and other larger studies appear to indicate a continuum of absolute C abundances, rather than discrete bands. Here we show that differences in the *heavy* element abundances as a function of the absolute carbon abundances ($[\text{C}/\text{H}]$) show similar plateau trends for the two sub-classes of CEMP stars. We note that larger samples may erase these plateaus and exhibit more continuous distributions around similar average values.

Comparison of the CEMP-*s* stars to AGB model yields (e.g., Cristallo et al. 2011) indicates that the progenitor AGB stars were primarily of the lower-mass variety (in agreement with Kennedy et al. 2011 and Bisterzo et al. 2012), while the NEMP star in our programme could be associated with a more massive AGB progenitor capable of producing large abundances of nitrogen relative to carbon. However, the $[\text{hs}/\text{ls}]$ ratio for this star agrees with values predicted for lower mass AGB stars ($\sim 2 M_{\odot}$). The two stars with low gravities (HE 1238–0836 and HE 2144–1832) appear to be pulsating variables, which could yield more trustworthy abundances if observed in a quiet phase. They could also be (intrinsic) AGB stars.

This study has shown that moderate-resolution, low-S/N X-shooter spectra are of sufficient quality to classify CEMP stars into sub-categories and extract information on their plausible astrophysical formation sites. This highlights an aspect of the X-shooter instrument that we consider very promising, the ability to obtain simultaneous measurements of C, N, Ba, and Sr very efficiently for a relatively large sample of faint stars. This is important, in particular for intermediate to low-metallicity $-2.5 < [\text{Fe}/\text{H}] < -1.0$ stars, a range we cover with our sample. This metallicity interval has been largely ignored in recent observational campaigns that concentrate on the most extreme metal-poor stars. Substantial and crucial information can be extracted at intermediate metallicity, where numerous stars of the halo system are found. For example, different *r*-process sites predict dispersions in stellar abundances of $[\text{Sr}/\text{H}]$ or $[\text{Ba}/\text{H}]$, as discussed by Cescutti & Chiappini (2014) and Hansen et al. (2012, 2014).

Acknowledgements. C.J.H. acknowledges support from research grant VKR023371 from the Villum Foundation, and both she and T.T.H. acknowledge support from Sonderforschungsbereich SFB 881. "The Milky Way System" (subproject A5) of the German Research Foundation (DFG). B.N. and C.J.H. thank Drs. J. Fynbo and D. Malesani for help with the X-shooter observations. B.N. acknowledges partial support by the National Science Foundation under Grant No. NSF PHY11-25915. T.T.H. thanks T. Masseron for line list information. T.C.B., C.R.K., and V.M.P. acknowledge partial funding of this work from grants PHY 08-22648; Physics Frontier Center/Joint Institute of Nuclear Astrophysics (JINA), and PHY 14-30152; Physics Frontier Center/JINA Center for the Evolution of the Elements (JINA-CEE), awarded by the US National Science Foundation. J.A. and B.N. acknowledge support from the Danish Council for Independent Research — Natural Sciences and the Carlsberg Foundation.

This publication has made use of the SIMBAD database, operated at CDS, Strasbourg, France, and of data products from the Two Micron All Sky Survey, which is a joint project of the University of Massachusetts and the Infrared Processing and Analysis Center/California Institute of Technology, funded by the National Aeronautics and Space Administration and the National Science Foundation.

References

- Abate, C., Pols, O. R., Karakas, A. I., & Izzard, R. G. 2015, *A&A*, 576, A118
- Allende Prieto, C., Barklem, P. S., Lambert, D. L., & Cunha, K. 2004, *A&A*, 420, 183
- Alonso, A., Arribas, S., & Martínez-Roger, C. 1999, *A&AS*, 140, 261
- Aoki, W., Beers, T. C., Christlieb, N., et al. 2007, *ApJ*, 655, 492
- Asplund, M., Grevesse, N., Sauval, A. J., & Scott, P. 2009, *ARA&A*, 47, 481

- Barklem, P. S., Christlieb, N., Beers, T. C., et al. 2005, *A&A*, 439, 129
- Beers, T. C. & Christlieb, N. 2005, *ARA&A*, 43, 531
- Beers, T. C., Flynn, C., Rossi, S., et al. 2007, *ApJS*, 168, 128
- Beers, T. C., Norris, J. E., Placco, V. M., et al. 2014, *ApJ*, 794, 58
- Bergemann, M., Hansen, C. J., Bautista, M., & Ruchti, G. 2012, *A&A*, 546, A90
- Bessell, M. S., Collet, R., Keller, S. C., et al. 2015, *ApJ*, 806, L16
- Bisterzo, S., Gallino, R., Straniero, O., Cristallo, S., & Käppeler, F. 2011, *MNRAS*, 418, 284
- Bisterzo, S., Gallino, R., Straniero, O., Cristallo, S., & Käppeler, F. 2012, *MNRAS*, 422, 849
- Bonifacio, P., Caffau, E., Spite, M., et al. 2015, *A&A*, 579, A28
- Caffau, E., Bonifacio, P., François, P., et al. 2011, *Nature*, 477, 67
- Carollo, D., Beers, T. C., Bovy, J., et al. 2012, *ApJ*, 744, 195
- Carollo, D., Freeman, K., Beers, T. C., et al. 2014, *ApJ*, 788, 180
- Castelli, F. & Kurucz, R. L. 2003, in *IAU Symposium*, Vol. 210, *Modelling of Stellar Atmospheres*, ed. N. Piskunov, W. W. Weiss, & D. F. Gray, 20P
- Cescutti, G. 2008, *A&A*, 481, 691
- Cescutti, G. & Chiappini, C. 2010, *A&A*, 515, A102
- Cescutti, G. & Chiappini, C. 2014, *A&A*, 565, A51
- Cescutti, G., Chiappini, C., Hirschi, R., Meynet, G., & Frischknecht, U. 2013, *A&A*, 553, A51
- Cescutti, G., Romano, D., Matteucci, F., Chiappini, C., & Hirschi, R. 2015, *A&A*, 577, A139
- Christlieb, N., Bessell, M. S., Beers, T. C., et al. 2002, *Nature*, 419, 904
- Christlieb, N., Green, P. J., Wisotzki, L., & Reimers, D. 2001, *A&A*, 375, 366
- Cole, A. A., Smecker-Hane, T. A., Tolstoy, E., Bosler, T. L., & Gallagher, J. S. 2004, *MNRAS*, 347, 367
- Cooke, R., Pettini, M., & Murphy, M. T. 2012, *MNRAS*, 425, 347
- Cooke, R., Pettini, M., Steidel, C. C., Rudie, G. C., & Nissen, P. E. 2011, *MNRAS*, 417, 1534
- Cristallo, S., Abia, C., Straniero, O., & Piersanti, L. 2015, *ApJ*, 801, 53
- Cristallo, S., Piersanti, L., Straniero, O., et al. 2011, *ApJS*, 197, 17
- Cutri, R. M., Skrutskie, M. F., van Dyk, S., et al. 2003, *VizieR Online Data Catalog*, 2246, 0
- Frebel, A., Aoki, W., Christlieb, N., et al. 2005, *Nature*, 434, 871
- Frebel, A., Christlieb, N., Norris, J. E., et al. 2006, *ApJ*, 652, 1585
- Frebel, A. & Norris, J. E. 2015, *ARA&A*, 53, 631
- Frischknecht, U., Hirschi, R., & Thielemann, F.-K. 2012, *A&A*, 538, L2
- Gallagher, A. J., Ryan, S. G., Hosford, A., et al. 2012, *A&A*, 538, A118
- Girardi, L., Bressan, A., Bertelli, G., & Chiosi, C. 2000, *A&AS*, 141, 371
- Goswami, A. 2005, *MNRAS*, 359, 531
- Goswami, A., Karinkuzhi, D., & Shantikumar, N. S. 2010, *MNRAS*, 402, 1111
- Hansen, C. J., Bergemann, M., Cescutti, G., et al. 2013, *A&A*, 551, A57
- Hansen, C. J., Montes, F., & Arcones, A. 2014, *ApJ*, 797, 123
- Hansen, C. J. & Primas, F. 2011, *A&A*, 525, L5
- Hansen, C. J., Primas, F., Hartman, H., et al. 2012, *A&A*, 545, A31
- Hansen, T., Hansen, C. J., Christlieb, N., et al. 2015, *ApJ*, 807, 173
- Henden, A. A., Levine, S., Terrell, D., & Welch, D. L. 2015, in *American Astronomical Society Meeting Abstracts*, Vol. 225, *American Astronomical Society Meeting Abstracts*, 336.16
- Herwig, F. 2005, *ARA&A*, 43, 435
- Hirschi, R. 2007, *A&A*, 461, 571
- Ito, H., Aoki, W., Beers, T. C., et al. 2013, *ApJ*, 773, 33
- Johnson, J. A., Herwig, F., Beers, T. C., & Christlieb, N. 2007, *ApJ*, 658, 1203
- Keller, S. C., Bessell, M. S., Frebel, A., et al. 2014, *Nature*, 506, 463
- Kennedy, C. R., Sivarani, T., Beers, T. C., et al. 2011, *AJ*, 141, 102
- Kobayashi, C., Tominaga, N., & Nomoto, K. 2011, *ApJ*, 730, L14
- Lee, Y. S., Beers, T. C., Masseron, T., et al. 2013, *AJ*, 146, 132
- Lee, Y. S., Beers, T. C., Sivarani, T., et al. 2008, *AJ*, 136, 2022
- Li, H., Aoki, W., Zhao, G., et al. 2015, *PASJ*, 67, 84
- Lucatello, S., Beers, T. C., Christlieb, N., et al. 2006, *ApJ*, 652, L37
- Lucatello, S., Tsangarides, S., Beers, T. C., et al. 2005, *ApJ*, 625, 825
- Maeder, A. & Meynet, G. 2015, *ArXiv e-prints*
- Maeder, A., Meynet, G., & Chiappini, C. 2015, *A&A*, 576, A56
- Marsteller, B., Beers, T. C., Rossi, S., et al. 2005, *Nuclear Physics A*, 758, 312
- Masseron, T., Johnson, J. A., Plez, B., et al. 2010, *A&A*, 509, A93
- Masseron, T., Plez, B., Van Eck, S., et al. 2014, *A&A*, 571, A47
- Masseron, T., van Eck, S., Famaey, B., et al. 2006, *A&A*, 455, 1059
- Matsuoka, K., Nagao, T., Maiolino, R., Marconi, A., & Taniguchi, Y. 2011, *A&A*, 532, L10
- Meynet, G., Ekström, S., & Maeder, A. 2006, *A&A*, 447, 623
- Nomoto, K., Kobayashi, C., & Tominaga, N. 2013, *ARA&A*, 51, 457
- Norris, J. E., Christlieb, N., Korn, A. J., et al. 2007, *ApJ*, 670, 774
- Norris, J. E., Ryan, S. G., & Beers, T. C. 1997, *ApJ*, 489, L169
- Piersanti, L., Cristallo, S., & Straniero, O. 2013, *ApJ*, 774, 98
- Pietrinferni, A., Cassisi, S., Salaris, M., & Hidalgo, S. 2013, *A&A*, 558, A46
- Placco, V. M., Beers, T. C., Ivans, I. I., et al. 2015, *ApJ*, 812, 109
- Placco, V. M., Beers, T. C., Roederer, I. U., et al. 2014a, *ApJ*, 790, 34
- Placco, V. M., Frebel, A., Beers, T. C., et al. 2013, *ApJ*, 770, 104
- Placco, V. M., Frebel, A., Beers, T. C., & Stancliffe, R. J. 2014b, *ApJ*, 797, 21
- Placco, V. M., Kennedy, C. R., Beers, T. C., et al. 2011, *AJ*, 142, 188
- Roederer, I. U. 2013, *AJ*, 145, 26
- Rossi, S., Beers, T. C., Sneden, C., et al. 2005, *AJ*, 130, 2804
- Schlegel, D. J., Finkbeiner, D. P., & Davis, M. 1998, *ApJ*, 500, 525
- Sivarani, T., Beers, T. C., Bonifacio, P., et al. 2006, *A&A*, 459, 125
- Sneden, C., Lucatello, S., Ram, R. S., Brooke, J. S. A., & Bernath, P. 2014, *ApJS*, 214, 26
- Sneden, C. A. 1973, PhD thesis, The University of Texas at Austin.
- Spite, M., Caffau, E., Bonifacio, P., et al. 2013, *A&A*, 552, A107
- Spite, M., Cayrel, R., Hill, V., et al. 2006, *A&A*, 455, 291
- Spite, M., Cayrel, R., Plez, B., et al. 2005, *A&A*, 430, 655
- Starkenburg, E., Shetrone, M. D., McConnachie, A. W., & Venn, K. A. 2014, *MNRAS*, 441, 1217
- Tominaga, N., Iwamoto, N., & Nomoto, K. 2014, *ApJ*, 785, 98
- Tominaga, N., Umeda, H., & Nomoto, K. 2007, *ApJ*, 660, 516
- Umeda, H. & Nomoto, K. 2003, *Nature*, 422, 871
- Venemans, B. P., McMahon, R. G., Walter, F., et al. 2012, *ApJ*, 751, L25
- Vernet, J., Dekker, H., D'Odorico, S., et al. 2011, *A&A*, 536, A105
- Wallerstein, G., Gomez, T., & Huang, W. 2012, *Ap&SS*, 341, 89
- Wanajo, S., Janka, H.-T., & Müller, B. 2011, *ApJ*, 726, L15
- Yong, D., Norris, J. E., Bessell, M. S., et al. 2013, *ApJ*, 762, 26
- Začs, L., Sperauskas, J., Grankina, A., et al. 2015, *ApJ*, 803, 17